The Astrophysical Journal, 1009:216 (10pp), 2026 October 1 https://doi.org/10.3847/1538-4357/ae9c2c
© 2026. The Author(s). Published by the American Astronomical Society.
OPEN ACCESS

Revisiting Neutrino Event Epochs for the Blazar PKS 0735+178 with TESS

Shubham Kishore[1], Alok C. Gupta[2], and Debanjan Bose[3]
[1] Indian Institute of Astrophysics, Bangalore (IIA), 560034, India; amp700151@gmail.com
[2] Aryabhatta Research Institute of Observational Sciences (ARIES), Manora Peak, Nainital 263001, India
[3] Central University of Kashmir, Ganderbal, 191131, India
Received 2026 May 15; revised 2026 August 3; accepted 2026 August 17; published 2026 September 29

Abstract

We present here the results of the optical light curve variability analysis of the blazars PKS 0735+178, in weeks-scale flare state, observed in three sectors with the Transiting Exoplanet Survey Satellite (TESS). The TESS observations in this study coincide with a well-known neutrino emission phase detected with four different neutrino observatories at multiple epochs in a narrow time window. We segmented the rising and decaying parts of the flare and individually analyzed their flux distribution, excess variance, variability timescale, and power spectral density (PSD). The source displayed an elevated excess variance of ∼25%, with a multimodal flux distribution (coherent in the rising and distorted in the decaying phase). The variability timescale analysis highlights a much faster decay than the rising scale, and the PSDs depict a nominal change in the power spectral slope. We discuss a likely connection in the optical variations and the neutrino events, and briefly explain a possible physical scenario for the observed optical flux behavior in view of previously discovered radio-band results.

Unified Astronomy Thesaurus concepts: Active galactic nuclei (16); Galaxies (573); Blazars (164); Optical astronomy (1776); High energy astrophysics (739)

1. Introduction

Flux variability is one of the defining characteristics of active galactic nuclei (AGNs), which are understood to possess accreting supermassive black holes (SMBHs) with masses in the range of $10^6-10^{10}M_{\odot}$. Blazars are a subclass of radio-loud AGNs that launch powerful, large-scale relativistic jets of plasma pointed toward the line of sight (LOS) ($\leqslant 10^{\circ}$) of the observer (e.g., C. M. Urry & P. Padovani 1995). BL Lacertae objects (BL Lacs) and flat-spectrum radio quasars (FSRQs) are jointly called blazars. In the composite ultraviolet (UV) to optical spectra, BL Lacs possess either absent or very weak narrow emission lines (equivalent width, EW, $\leqslant 5$ Å), whereas FSRQs show broad and strong emission lines.

Blazars display large flux and spectral variability on diverse timescales throughout the observable electromagnetic (EM) bands and show substantial polarization that is also often variable in the radio, optical, and X-ray bands (e.g., M. L. Lister et al. 2018; A. C. Gupta et al. 2019; H. L. Marshall et al. 2024, and references therein). Blazar variability having timescales of a few minutes to less than a day is often called microvariability (H. R. Miller et al. 1989), intraday variability (IDV; S. J. Wagner & A. Witzel 1995), or intranight variability (G. Krishna et al. 1995). Variability occurring over a few days to weeks is known as short-term variability (STV), while that occurring over periods longer than months is called long-term variability (LTV; A. C. Gupta et al. 2004). The nature of blazar light curves (LCs) in the whole EM spectrum is mostly nonlinear, stochastic, and aperiodic (e.g., P. Kushwaha et al. 2017).

The emission from blazars in the whole EM spectrum is predominantly nonthermal. The spectral energy distributions (SEDs) of blazars display a characteristic double-humped structure in the $\log \nu$ versus $\log \nu F_{\nu}$ diagram (G. Fossati et al. 1998). The lower-energy hump lies in the radio to UV or, sometimes, soft X-rays, most likely due to polarized synchrotron emission from relativistic electrons in the hot plasma in a magnetic environment. Depending on the location of the peak of this lower-energy hump in the mentioned EM regime, the blazars are often termed low-, intermediate-, or high-synchrotron peaked (LSP: $\nu_{\rm peak} < 10^{14}$ Hz, ISP: 10^{14} Hz $< \nu_{\rm peak} < 10^{15}$ Hz, and HSP: $\nu_{\rm peak} > 10^{15}$ Hz) blazars (A. A. Abdo et al. 2010). The higher-energy hump covers X-rays to γ-rays, which is most likely due to inverse Compton emission from the interaction of relativistic electrons (under the so-called "leptonic model") and the low-energy seed photons. When the seed photons originate from the synchrotron emission itself, the mechanism is termed synchrotron self-Compton (SSC); otherwise, it is called the external Compton (EC) mechanism.

Beyond leptonic processes, the high-energy component is often attributed to hadronic interactions. In this scenario, γ-rays can be produced from the decay of neutral pions (π^0) in proton–photon or proton–proton collisions (K. Mannheim 1993). Alternatively, these high-energy γ-rays may be generated through synchrotron emission from relativistic protons in magnetized media (F. A. Aharonian 2000). A new perspective on the nonthermal processes in our Universe was made possible by the IceCube Neutrino Observatory's 2013 discovery of high-energy neutrinos of cosmic origin (M. G. Aartsen et al. 2018). The origin of ultra-high-energy cosmic rays (UHECRs), the Universe's most energetic particles with energies more than 10^{18} eV, has long been a mystery (B. R. Dawson et al. 2017). A largely extragalactic origin is supported by the observed distribution of their arrival directions in the sky (Pierre Auger Collaboration et al. 2017). It was predicted more than 1.5 decades ago that neutrino emission can be detected from some blazars (A. Y. Neronov & D. V. Semikoz 2002). On 2017 September 22, the IceCube neutrino observatory detected the first likely neutrino event from the blazar TXS 0506+056 at energy ∼290 TeV, which was

Original content from this work may be used under the terms of the Creative Commons Attribution 4.0 licence. Any further distribution of this work must maintain attribution to the author(s) and the title of the work, journal citation and DOI.

identified as IceCube-170922A (S. Ansoldi et al. 2018; IceCube Collaboration et al. 2018). The prerequisites for neutrino emission from blazars are through proton–photon interactions, i.e., a situation where the shock may accelerate protons to relativistic energies, with the target photons (G. F. Paraschos et al. 2025). Parsec-scale relativistic jets play an important role in neutrino production in blazars. The relativistic protons present in the jet collide with the low-energy photons (optical/UV/X-ray) present in the surrounding ambient medium and produce pions. The decay of charged pions ultimately produces high-energy neutrinos. A detailed model and explanation is given in A. V. Plavin et al. (2021).

PKS 0735+178 at $z = 0.45 \pm 0.06$ (K. Nilsson et al. 2012) was first optically identified by G. M. Blake (1970) and classified as a BL Lac (R. F. Carswell et al. 1974). The source is optically bright, its host galaxy is unresolved in optical imaging, and the optical spectrum is a featureless continuum (R. F. Carswell et al. 1974). The source has been extensively studied in the optical bands in the search for flux variability on the diverse timescales that were often detected (e.g., S. Ciprini et al. 2007; A. C. Gupta et al. 2008; A. Goyal et al. 2009, 2017; Y. Fang et al. 2022, and references therein). The source has displayed a high degree of optical and near-infrared polarization up to 35% (e.g., A. R. G. Mead et al. 1990; L. O. Takalo 1991; L. Valtaoja et al. 1991, 1993; L. O. Takalo et al. 1992; L. Tommasi et al. 2001; B. J. Wills et al. 2011, and references therein). There are detections of periodic and quasiperiodic oscillations on diverse timescales in optical LCs of the source (J. H. Fan et al. 1997; B. Qian & J. Tao 2004; S. Ciprini et al. 2007; S. Kishore et al. 2026). Multiwavelength (MW) variability, cross correlation in different EM bands, and SEDs are also studied for the source (A. Goyal et al. 2017; Y. Fang et al. 2022; N. Sahakyan et al. 2023).

During early 2021 December, the source PKS 0735+178 was found to be in the spatial vicinity ($\sim 2.05^{\circ}$; S. Garrappa et al. 2021) of a neutrino event (IceCube-211208A[4]) of $\sim$171 TeV. The event triggered inspection of the related sky region with other facilities, such as with Baikal (43 TeV; Z. A. Dzhilkibaev et al. 2021), Baksan (>1 GeV; V. B. Petkov et al. 2021), and KM3NeT (18 TeV; F. Filippini et al. 2022), while it was undergoing its largest γ-ray, optical, and soft X-ray flare observed since the launch of the Fermi satellite in 2008 (N. Sahakyan et al. 2023). Preliminary analysis indicates that on 2021 December 8, the source was observed with a daily averaged flux ($E > 100$ MeV) being about 5 times greater than the average value indicated in the fourth Fermi-LAT source catalog (4FGL-DR2), and its peak daily flux value was already observed to be about 10 times greater than the average 4FGL-DR2 flux on 2021 December 4. The neutrino event was reported by four observatories during the 2021 December flare exhibited in the source in the γ-ray, X-ray, UV, infrared, and optical bands (A. Acharyya et al. 2023). R. Prince et al. (2024) analyzed the 100 day γ-ray and X-ray data, which spanned 10 days around the neutrino event, and then generated broadband SEDs and modeled them by fitting synchrotron and SSC models and invoking photohadronic ($p\gamma$) interactions inside the jet. The SED of the source can be well modeled under the pure leptonic emission scenario, according to another MW SED analysis conducted during the neutrino event. This is likely because the hadronic emission contribution is subdominant to the leptonic process (A. M. Bharathan et al. 2024). By using Very Long Baseline Interferometry polarized light images of PKS 0735+178, no new jet ejection component was observed during that narrow time frame of the neutrino-emission event (G. F. Paraschos et al. 2025). S. Britzen et al. (2026) examined long-term Very Long Baseline Array observations of the source, having 40 epochs of 15 GHz data (1995.27–2025.02) and 116 epochs of 43 GHz data (2008.62–2025.22), which also covered the time of the neutrino detections. They proposed that jet precession aligns the more nuclear parts of the jet into loops and rings due to gravitational lensing by a known intervening absorption system ($z = 0.424$). The MW variability of the source, for which LCs span the radio (1–230 GHz), optical, and Fermi-LAT γ-ray bands over about 3 decades, was recently reported. Delays from 0 to 1200 days increase toward lower frequencies in the associated LCs, which is compatible with emission from an opacity-stratified jet (T. V. Mufakharov et al. 2026).

In this paper, we present results of the time-domain analysis of a high-cadence, densely sampled LC of the blazar PKS 0735+178 that was fortunately within the field of view of the Transiting Exoplanet Survey Satellite (TESS) during the well-recognized neutrino event in early 2021 December. No known previous study of this source utilized such a high-cadence sampled dataset over an appreciable duration covering all three cases of the pre-, mid-, and postevent epochs, which is helpful in getting the temporal aspects of the source during the neutrino-emission epochs.

The paper is structured as follows. In Section 2, we discuss the TESS data acquisition and reduction that we carried out. Sections 3–6 provide descriptions of the data analysis employed and the results in the present work. Section 7 includes the discussions and conclusions.

2. Data Acquisition and Light Curves

Readers are referred to key papers such as G. R. Ricker et al. (2014), J. M. Jenkins et al. (2016), and J. D. Twicken et al. (2020) for the details of the instruments used and the data achieved. The details of the TESS instruments are available online[5] and have been briefly discussed in S. Kishore et al. (2023), along with a description of the two types of fluxes that TESS offers. Also discussed in our previous paper are the parameters that we used in the data reduction: an overfitting metric, an underfitting metric, and a regularization parameter (α), along with their optimum values for good data reduction. Briefly, TESS offers two types of flux values: the SAP_FLUX (summing all pixel values in a predefined aperture corresponding to a source) and its detrended form, PDCSAP_FLUX. Both of these flux values can be further processed to remove any persisting instrumental artifacts. However, the detrending can majorly affect any genuine flux variation of the source objects, particularly when the sources display stochastic LCs, variable on all timescales, i.e., blazars (or AGNs). Evidence of this effect can be seen as jumps in the mean sectorial flux levels of the source when observed in multiple sectors. In such cases, the LC obtained with the differential photometry can very efficiently guide the appropriateness of the SAP_FLUX and PDCSAP_FLUX and their processed versions for a particular sector.

[4] https://gcn.nasa.gov/circulars/events/icecube-211208a

[5] https://heasarc.gsfc.nasa.gov/docs/tess/

It is important to note here that the pixel size for the TESS CCD is large enough to get contaminated by nearby objects, and the actual variability of the source under probe can be affected by such extraneous contributions. This is also the case for PKS 0735+178, which is accompanied by two nearby faint objects. We tested the variability of these two accompanying objects by inspecting the *r*-filter data of the Zwicky Transient Facility (ZTF), which is within the TESS bandpass filter system. Employing a differential photometry on the source[6] and its two accompanying objects (at left and right) of the ZTF data, using a comparison object denoted "D" (chosen because of its less crowded location, see P. S. Smith et al. 1985), we found no obvious variations in the flux values of the two side objects; hence, any variation observed in the TESS differential LC of the source can be immediately attributed to source-intrinsic variation. Since the comparison object "D" has no nearby contaminating objects, there is no need for such contamination inspection for "D." After this basic scrutiny, we generated the aperture photometric LCs of the source and the comparison object, along with an estimation of the background flux counts from the 11 × 11 pixel cutouts of the full-frame images centered at the source and "D," provided by TESS. The "D" flux values were first background subtracted and further divided by the sectoral median flux values to obtain a set of normalized flat values. The aperture photometric LC of the source is then subtracted by the background counts, followed by division by the flats to get a differential LC of the source. Figure A1 in the Appendix represents the obtained differential LCs along with the background flux, normalized flat (using "D"), and raw flux of the source for each of the three sectors. We find that though the SAP_FLUX, PDCSAP_FLUX, and their processed version can comprehend microvariability patterns, the trends for the STV analysis seen in the obtained differential LCs are best depicted by the SAP_FLUX only. Figure A2 highlights the comparisons of the LCs obtained differently, with the differential LCs for the three sectors. Previously, too, the SAP_FLUX has been seen to be equally useful for variability studies (e.g., C. M. Raiteri et al. 2021). Hence, we directly utilized the SAP_FLUX without any further detrending. However, in our analysis, all the LCs were made free of local outliers exceeding 3 times the local 1 day standard deviation. The source PKS 0735+178 has been observed by TESS in five sectors: 44, 45, 46, 71, and 72, out of which `LightCurveFiles` were available only for sectors 44, 45, and 46, which include the SAP_FLUX and the PDCSAP_FLUX. The current study focuses on the LCs obtained in these three sectors only, which cover the peculiar neutrino event. Figure 1 presents the composite LC of the three sectors thus obtained.

3. Flux Distribution

The composite LC, as shown in Figure 1, depicts a strong flare event spanning around 75 days. For simplicity here, we have considered the starting epoch of the flare to be ∼BTJD 2504.3, where the flux values reach a global minimum in the complete LC (∼120 e^- s^{-1}). Visual inspection of the LC indicated that the object undergoes a rapid flux increase, reaching a maximum count of ∼375 e^- s^{-1} at ∼BTJD 2558.1, followed by an even faster decay. Flux distribution is one of the defining properties of accretion-powered sources, as AGNs, often showing normal or lognormal distribution (e.g., P. Kushwaha et al. 2016, 2017, and references therein). The observed flux distribution can be interpreted within the standard framework of variability in accreting systems, where lognormal flux distributions and linear rms–flux relations arise naturally from multiplicative processes in the accretion flow. This behavior has been extensively established in X-ray binaries and AGNs (e.g., P. Uttley et al. 2002, 2005), and is often taken as evidence for inwardly propagating fluctuations in the disk. In this context, the flux distribution of PKS 0735 +178 is consistent with stochastic variability driven by such multiplicative processes. The symmetric/asymmetric nature of the profile can be utilized to find the dominance of the cooling process during the LC variations (M. Chiaberge & G. Ghisellini 1999). For a well-resolved flare, we also expect the distribution of the flux to have a normal or lognormal nature. Assuming that the flare spans from ∼BTJD 2504.3 to ∼BTJD 2578.7, we evaluated the flux distribution between these epochs of the 2 minute cadence LC and present the estimated profile in Figure 2. The profile has been found to be uneven, so we also evaluated the distribution for rising and decaying segments individually (see Figure 2). We find that the distribution for the rising part consists largely of well-separated (equidistantly located within uncertainties), distinct Gaussian profiles, and the unevenness in the profile for the complete LC is mainly due to the flux distribution of the decaying part. We also note that the high flux values (in the vicinity of ∼350 e^- s^{-1}) are mainly found within the distribution of the decaying portion of the LC. This is highly likely due to the selection bias introduced by the partition of the LC into rising and decaying regions, which was performed via visual inspection.

4. Excess Variance

Accompanied by an additional variability because of the instrumental measurement errors in the observations, the typical variance test can lead to erroneous results. Since flux variability acts as one of the elementary properties of a typical blazar across all EM bands, incorporating the intrinsic measurement uncertainties becomes crucial. The excess variance method assertively takes care of this uncertainty in quantifying the variability. Given as

$$F_{\rm var} = \sqrt{\frac{S^2 - \overline{\sigma_{\rm err}^2}}{\bar{x}^2}}, \tag{1}$$

$$(F_{\rm var})_{\rm err} = \sqrt{\left[\sqrt{\frac{1}{2n}}\frac{\overline{\sigma_{\rm err}^2}}{F_{\rm var}\bar{x}^2}\right]^2 + \left[\sqrt{\frac{\overline{\sigma_{\rm err}^2}}{n}}\frac{1}{\bar{x}}\right]^2}, \tag{2}$$

the fractional rms variability amplitude ($F_{\rm var}$), or the square root of normalized excess variance, and its corresponding uncertainty have been computed as in S. Vaughan et al. (2003). Here, $S^2 - \overline{\sigma_{\rm err}^2}$, $\bar{x}$, and n are the uncertainty corrected variance, mean flux, and number of data points, respectively. Over the span from BTJD 2504.3–2578.7 of the 2 minute cadence data, the average flux is 209.23 e^- s^{-1}, and the source exhibits an overall variability amplitude of 25.16% ± 0.01%. The very small associated uncertainty marks the statistical

[6] Field of view of PKS 0735+178 (www.lsw.uni-heidelberg.de/projects/extragalactic/charts/0735+178.html).

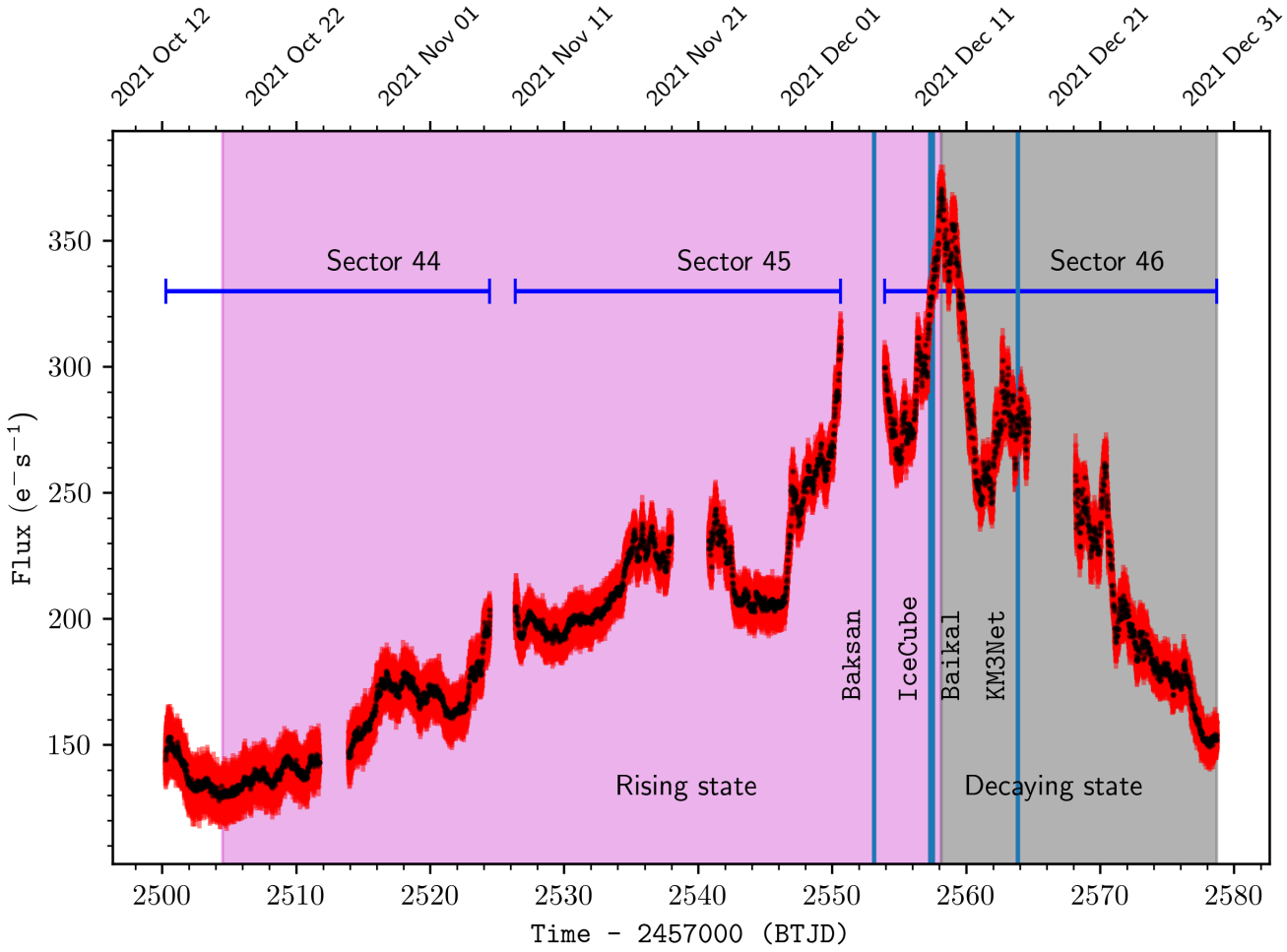


Figure 1. LC of the blazar PKS 0735+178, observed in the three continuous indicated sectors (44, 45, and 46); the red LC has a 2 minute cadence, and the black LC is 30 minute binned; both have been used in the analyses.

errors only and does not include the realization scatter intrinsic to a single stochastic LC segment.

5. Variability Timescale

As in S. Kishore et al. (2024), we utilized the halving/doubling time approach to estimate the variability timescale of the rising (∼BTJD 2504.3–2558.1) and decaying (∼BTJD 2558.1–2578.7) portions individually, expecting them to follow a normal Gaussian distribution. We put similar selection criteria for timescale estimation, choosing only those data-point pairs whose flux difference was 3 times more than the corresponding uncertainty. As the number of such eligible pairs behaves like n^2 (n being the number of data points), we note that a 30 minute (rather than 2 minute) binned LC of the object was utilized to reduce the computational strain due to an extremely large number of eligible pairs for timescale estimation. The halving/doubling timescales are given as

$$F(t) = F(t_0)2^{(t-t_0)/\tau} \qquad (t > t_0). \tag{3}$$

Figure 3 includes the doubling and halving timescales of the rising and decaying portions of the flare, respectively. We find that the obtained distributions have a major contribution from a single timescale, but unlike in S. Kishore et al. (2024), they cannot be completely satisfied by single Gaussian functions, showing a multimodal profile. The most probable timescales dictating the flux variations for the two regions are found to be 43 ± 6 and 17 ± 3 days, which simply indicates a much faster decay rate than the rising.

6. Periodogram Analysis

The power spectral density (PSD) profile offers useful information regarding the source of variations observed in the LC. AGNs (or blazars) often show a power-law (PL) PSD profile ($P(\nu) = A\nu^{-\alpha}$) with the value of α within the vicinity of 2, although high values to up to 3.3 have also been reported (e.g., R. F. Mushotzky et al. 2011; T. T. Shimizu & R. F. Mushotzky 2013; M. Revalski et al. 2014; K. L. Smith et al. 2018, and references therein); however, other profile structures have also been discovered, including bending PLs (BPLs; e.g., O. González-Martín & S. Vaughan 2012 and references therein). The PSD characteristic timescales have also been observed to be related to the central black hole mass (I. M. McHardy et al. 2006).

For PSD analysis of the LC in Figure 1, we utilized the 2 minute cadence LC. The rising and decaying parts of the flare were first made devoid of big data gaps using linear

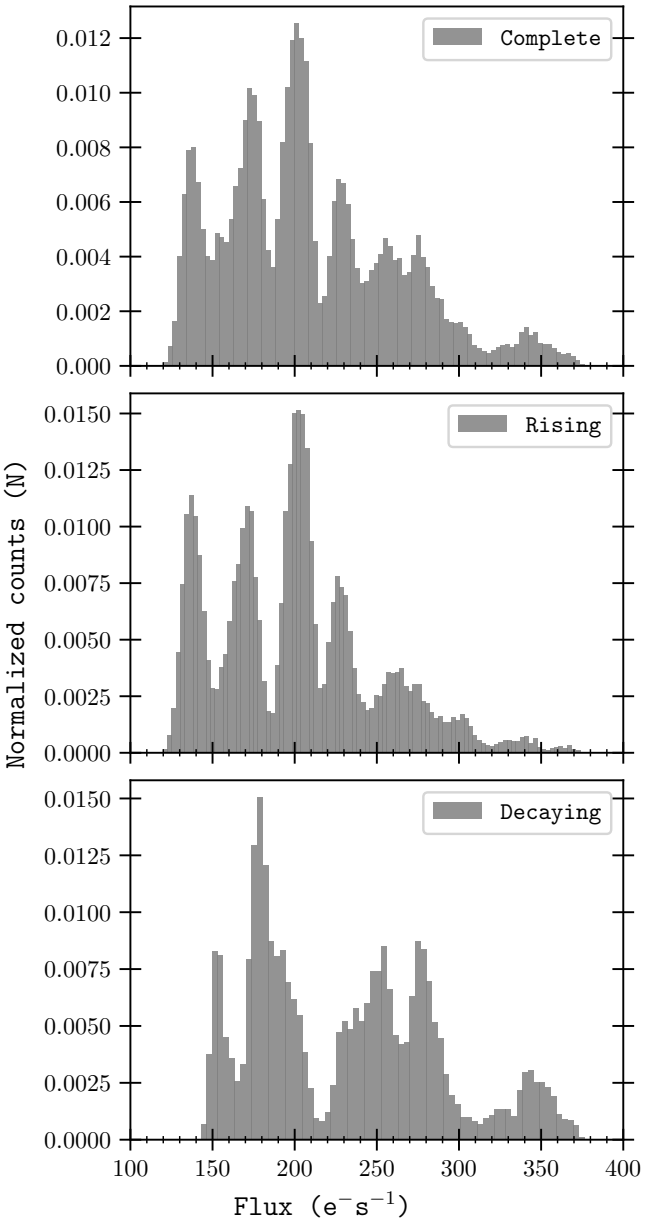


Figure 2. Top, middle, and bottom: flux distributions of complete flare portion (highlighted in magenta and gray regions in Figure 1), rising part (magenta region), and decaying portion (gray region), respectively.

interpolation to make the segments uniform and get rid of spectral leakages. We then implemented the generalized Lomb–Scargle periodogram (GLSP; see M. Zechmeister & M. Kürster 2009 and references therein) individually to both the rising and decaying part of the flare to inspect the variations in either the PSD shape or the spectral index, testing them with three different models (with α as spectral slope, following O. González-Martín & S. Vaughan 2012; D. Emmanoulopoulos et al. 2013):

M_1 (simple PL, "SPL")

$$P(\nu) = A\nu^{-\alpha_1} + c, \tag{4}$$

M_2 (bending PL, "BPL1")

$$P(\nu) = A\nu^{-1}\left[1 + \left(\frac{\nu}{\nu_b}\right)^{\alpha_1 - 1}\right]^{-1} + c, \tag{5}$$

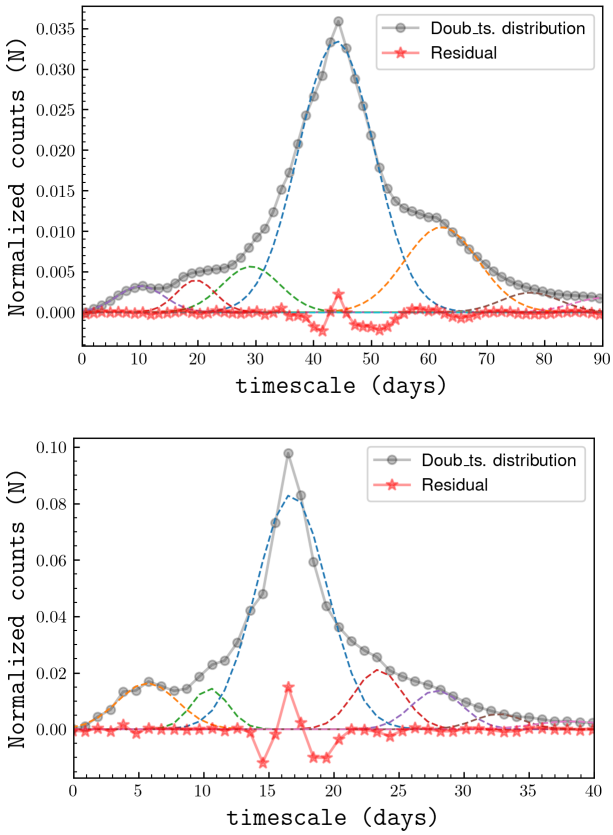


Figure 3. Halving/doubling timescale distribution for the rising phase (upper panel) and the decaying phase (lower panel); the distributions have been fit using a linear combination of multiple Gaussian profiles to infer the relative contributions of peculiar timescales.

and M_3 (bending PL, "BPL2")

$$P(\nu) = A\nu^{-\alpha_2}\left[1 + \left(\frac{\nu}{\nu_b}\right)^{\alpha_1 - \alpha_2}\right]^{-1} + c, \tag{6}$$

where the free parameters A, α_1, α_2, ν_b and c are the normalization, spectral indices, bending frequency, and an additive constant, respectively. The above three models respectively have three, four, and five free parameters. The best model selection describing the PSD was done using minimization of the Bayesian information criterion (BIC), which relies on the log-likelihood statistic given as

$$\mathrm{BIC} = k \cdot \ln(n) \; - \; \mathcal{L} \tag{7}$$

and the log-likelihood statistic is given as

$$\mathcal{L} = -2\sum_j \frac{I_j}{P_j} + \log P_j, \tag{8}$$

where I_j and P_j represent the estimated and the fitted PSD of the LC, respectively. Following S. Vaughan (2005, 2010), individual model parameters are estimated by minimizing S ($\equiv -\mathcal{L}$), and the associated uncertainty limits can be estimated under the condition $\Delta S = S(\theta) - S_{\min} \leqslant 2.71$, corresponding to 90% confidence limits (see Appendix A of S. Vaughan 2005), where θ represents model parameters.

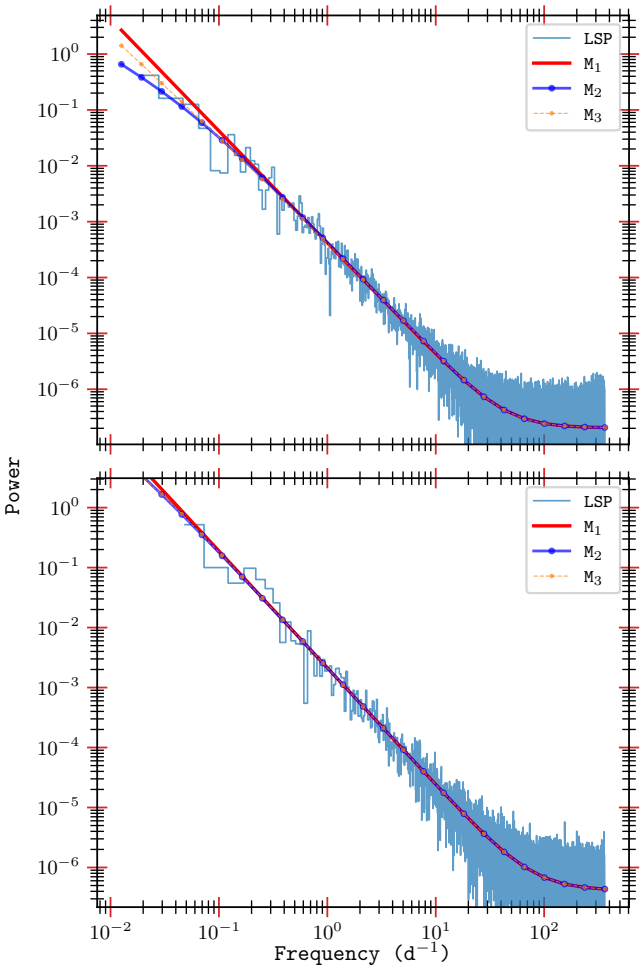


Figure 4. GLSP results for the rising (upper panel) and the decaying (lower panel) parts. Note: The use of LSP in the labels of these plots denotes the generalized Lomb–Scargle periodogram, i.e., GLSP, and is specific to these plots only.

Figure 4 includes the GLSP results of the rising and decaying parts of the LC. Considering the BIC criteria, we find that both the rising and decaying parts can be illustrated with the simple PL (SPL) model—M_1. Table 1 includes the GLSP fitting parameters with the SPL, demonstrating a fractional variation in the PL slopes for the rising and decaying parts. Similar to the case of fractional variability amplitude, we again note that estimated parameter uncertainties represent statistical or fit errors only, without including the realization scatter owing to the stochastic nature of the LC segment.

7. Discussion and Conclusion

In this work, we carried out high-cadence optical LC analysis of the blazar PKS 0735+178, which was observed from TESS in early 2021 December when the neutrino event association by the source was reported (e.g., A. Acharyya et al. 2023; N. Sahakyan et al. 2023, and references therein). The presented data are the densest optical sampling of the flare reported hitherto, temporally coincident with the alerts: Baksan, IceCube, Baikal, and KM3NeT at ∼BTJD 2553.1, 2557.3, 2557.5, and 2563.9, respectively. The main motivation of the present study is to see how the optical flux of the blazar during the neutrino detection epoch compares with the pre- and postneutrino detections. We find a highly resolved enhanced optical flux during the time period of the reported

Table 1
GLSP Fitting Parameters for the Rising and Decaying Epochs of the Flare; the Uncertainties Represent the Maximum of Upper and Lower Uncertainty Values

Parameters	Rising	Decaying
Norm. (A)	$(4.17 \pm 0.15) \times 10^{-4}$	$(2.13 \pm 0.10) \times 10^{-3}$
Spec. index (α_1)	2.00 ± 0.01	1.95 ± 0.01
Offset (c)	$(2.03 \pm 0.03) \times 10^{-7}$	$(4.15 \pm 0.10) \times 10^{-7}$

Note. BIC favors characterizing the rising and decaying epochs with M_1 (SPL).

neutrino alerts compared to the pre- and postalert phases. The former three alerts lie in the rising phase, with IceCube and Baikal alerts very near to the optical maxima (∼BTJD 2558.3), while the alert with the KM3Net appears in the decaying phase of the flare. While such high optical states are a common feature of flaring blazars and do not, by themselves, establish a physical association with neutrino emission, they are consistent with conditions conducive to neutrino production. In particular, an enhanced optical state may reflect increased particle acceleration and enhanced target photon densities within the emission region, both of which are key ingredients in leptohadronic scenarios. The TESS optical LC of the blazar PKS 0735+178 is displayed in Figure 1. The total LC covers the duration of BTJD ∼ 2500 to ∼2580. In this duration the flux of the source has systematically increased from ∼120 to ∼370 e^- s^{-1} from BTJD ∼ 2502 to ∼2559, followed by a sharp decrease from ∼370 to ∼140 e^- s^{-1} from BTJD ∼ 2559 to ∼2580. MW investigations for the SED have been carried out previously to infer the emission properties covering γ-ray to radio bands (A. Acharyya et al. 2023; N. Sahakyan et al. 2023) and the possibilities of different models satisfying the observed neutrino events, although they lack a much denser dataset as achieved with the TESS. A recent study by Y.-S. Kim & J.-Y. Kim (2025) of this blazar in the radio regime (15 and 43 GHz) using very-long-baseline interferometry found ejection of a new component (C2) from the core, which crossed a comparatively slowly moving component (C1) along the jet. Using linear back-extrapolation, they estimated that ejection of C2 with a superluminal apparent speed of ∼4.2c is 172.7 ± 34.5 days before the epoch of IceCube-211208A (see footnote 4). With the available TESS data, assuming that ejection occurred at around the minima of the LC, this ejection epoch lies at around 50 days before the IceCube-211208A. The difference in these two ejection epochs may be due to the fact that C2 started with an even higher apparent speed. This assessment can only be vaguely declared due to the lack of TESS observations of this source at earlier epochs. The multiple detections or alerts of neutrino events are between BTJD ∼ 2553 and ∼2564, which are apparently the epochs when C2 crossed C1. This leads to two possibilities for the neutrino-emission region. The first case suggests that it is produced near the core with a possible time lag in which the optical flux leads neutrino detection, due to which the source flux starts increasing, and then after detection of the neutrino event, the flux declines sharply. The second case suggests that neutrino emission is favored only after reaching a certain energy level or plasma density for any responsible radiation process during the interaction of C2 with C1. The latter cause is more plausible because of the very narrow time window of the neutrino detection, with epochs coinciding with those of optical maxima.

Owing to the simple causality relation, the most probable variability timescales (here, the doubling timescale $\equiv \tau_{\rm var}$) estimated for the rising phase (assuming that C2 is responsible for the flare) of the flare can be utilized to put limits on the corresponding emission region size (R), given as

$$R \leqslant \frac{c\ \tau_{\rm var}\ \delta}{1+z}, \tag{9}$$

where δ is the Doppler factor. Considering $\delta = 7.59 \pm 3.15$ and $z = 0.45 \pm 0.06$ (K. Nilsson et al. 2012; Y.-S. Kim & J.-Y. Kim 2025), we find it to be $(5.8 \pm 2.6) \times 10^{17}$ cm. The composite LC is seen to have a flaring asymmetric profile with a comparatively slower rise and faster decay (SRFD) that provides vital clues about particle acceleration, energy loss, and the physical environment inside relativistic jets. The SRFD profile is often attributed to the contrast between slow, sustained particle acceleration within the jet and rapid radiative energy losses, which can arise from changes in the jet structure, such as variations in the Doppler factor, relativistic magnetic reconnection events, or geometric effects like jet precession (e.g., M. Chiaberge & G. Ghisellini 1999; Z. Shah et al. 2021; P. M. Kouch et al. 2026).

Although it cannot be uniquely constrained by the current data, and the above alternative explanations are viable, we propose here one of the probable scenarios for the displayed optical behavior, including a system consisting of an emission core near the central black hole capable of injecting plasmas in the magnetized jet, apparent as distinct components (C1 or C2) in the radio images. C1 propagates at a slower speed along the jet, and at a later stage, C2 is ejected from the core at a higher superluminal speed, which later crosses C1. The flare observed here seems to be mainly due to the newly injected component C2. Visual inspection of the flux distribution of the rising part of the flare suggests that there are several flux states during the rise. In addition, the flux differences between consecutive humps in the distribution are found to be nearly equal (within corresponding uncertainties). Considering the proposed scenario, this simply suggests that injections of nearly comparable quantities of plasma from the proposed emission core to the jet are occurring at regular intervals of time, which collectively appear as a single component, C2, as it propagates along the jet and reaches the upcoming knot, C1. Looking at the doubling timescale distribution of the rising part, two major humps (at $\sim$43 and $\sim$61 days) can be perceived. In the current scenario, the bigger hump may correspond to the overall flux doubling rate of the rise, while the smaller one appears because plasma gets injected in chunks, after particular intervals, delaying the rise and giving an additional, longer rising timescale. As C2 approaches C1, it is possible that disruption of the compact individual components has happened, and the accumulated plasma is fragmented into an ensemble of randomly moving and variably sized fragments. This aligns with our proposed notion in the manner that multiple dissimilar-sized plasma blobs will have their own individual flux states and will be reflected as a very irregularly shaped overall flux distribution, as seen for the decaying portion in Figure 2. The continuous increase in the full-width half-maxima of C1 and C2 in the radio images of Y.-S. Kim & J.-Y. Kim (2025) aligns with this idea of plasma evolution. Also, because these small fragments have now rather random movements, there will be a major decrease in the Doppler factor (because of variation in the viewing angle of the fragmented plasma motion), causing a much sharper flux decay. This would be consistent with the halving timescale of the decay (Figure 3), which is much less than that of the rising part. A meager variation in the spectral slope (α) suggests that fragmented plasma blobs have a similar particle distribution to that of the parent distribution in the flux frozen state, differing only in their respective sizes.

More than 2 decades ago, it was predicted that some blazars may be neutrino-loud, and the small sample of potential sources mentioned was dominated by strong TeV-emitting HBL (same as HSP) blazars (A. Y. Neronov & D. V. Semikoz 2002). To date, neutrino emissions have only been reported from four blazars: TXS 0506+056, PKS 1424+240, GB6 J1542+6129, and PKS 0735+178, and most of them do not belong to strong TeV-emitting HBL blazars (N. Sahakyan et al. 2023). In contrast to "real" BL Lacs, which are intrinsically featureless or very weak emission-lined, P. Padovani et al. (2017, 2019, 2022) found that all four neutrino-emitting blazars are masquerading BL Lacs, namely FSRQs, whose emission lines are overwhelmed by an extremely bright, Doppler-boosted jet. As high-excitation galaxies (HEGs) with intrinsically strong emission lines dominating their composite optical/UV spectra, masquerading BL Lacs benefit from a number of radiation fields outside the jet, such as the dusty torus, photons reprocessed in the broad-line region (BLR), and the accretion disk, which may increase neutrino production by giving the protons more targets. PKS 0735+178 has been discussed as a potential neutrino-emitting blazar in several recent multimessenger studies. Detailed broadband and leptohadronic modeling efforts (e.g., A. Acharyya et al. 2023; N. Sahakyan et al. 2023; G. F. Paraschos et al. 2025) indicate that, while hadronic scenarios can reproduce the observed SED, the predicted neutrino flux is typically low and strongly model dependent. Even leptonic models can also adequately explain the EM emission. We note that the temporal proximity of the observed EM activity to the reported neutrino event may suggest a possible physical connection, potentially within a common hadronic emission framework. However, given the limited statistical significance and the absence of simultaneous multimessenger constraints, such an association remains tentative. Currently, the sample of neutrino-emitting blazars is very tiny, and we need more time to detect neutrino emission from many more blazars before we can make a conclusive statement. Alternative explanations, including a chance coincidence, cannot be excluded. Therefore, the neutrino-emission link should be regarded as suggestive rather than conclusive, pending further observational evidence.

Acknowledgments

We thank the reviewer for very useful comments, which helped us to improve the manuscript. This paper includes data collected with the TESS mission, obtained from the Mikulski Archive for Space Telescopes (MAST) data archive at the Space Telescope Science Institute (STScI). Funding for the TESS mission is provided by the NASA Explorer Program. STScI is operated by the Association of Universities for Research in Astronomy, Inc., under NASA contract NAS5–26555. The specific observations analyzed can be accessed via doi: 10.17909/q0dp-x410.

Software: lightkurve (Kurve Collaboration et al. 2018), SciPy (P. Virtanen et al. 2020), PyAstronomy (S. Czesla et al. 2019).

Appendix

Here, we present the differential LCs obtained in the three sectors (Figure A1) and the comparison of the differential LCs with those obtained with other methods (Figure A2).

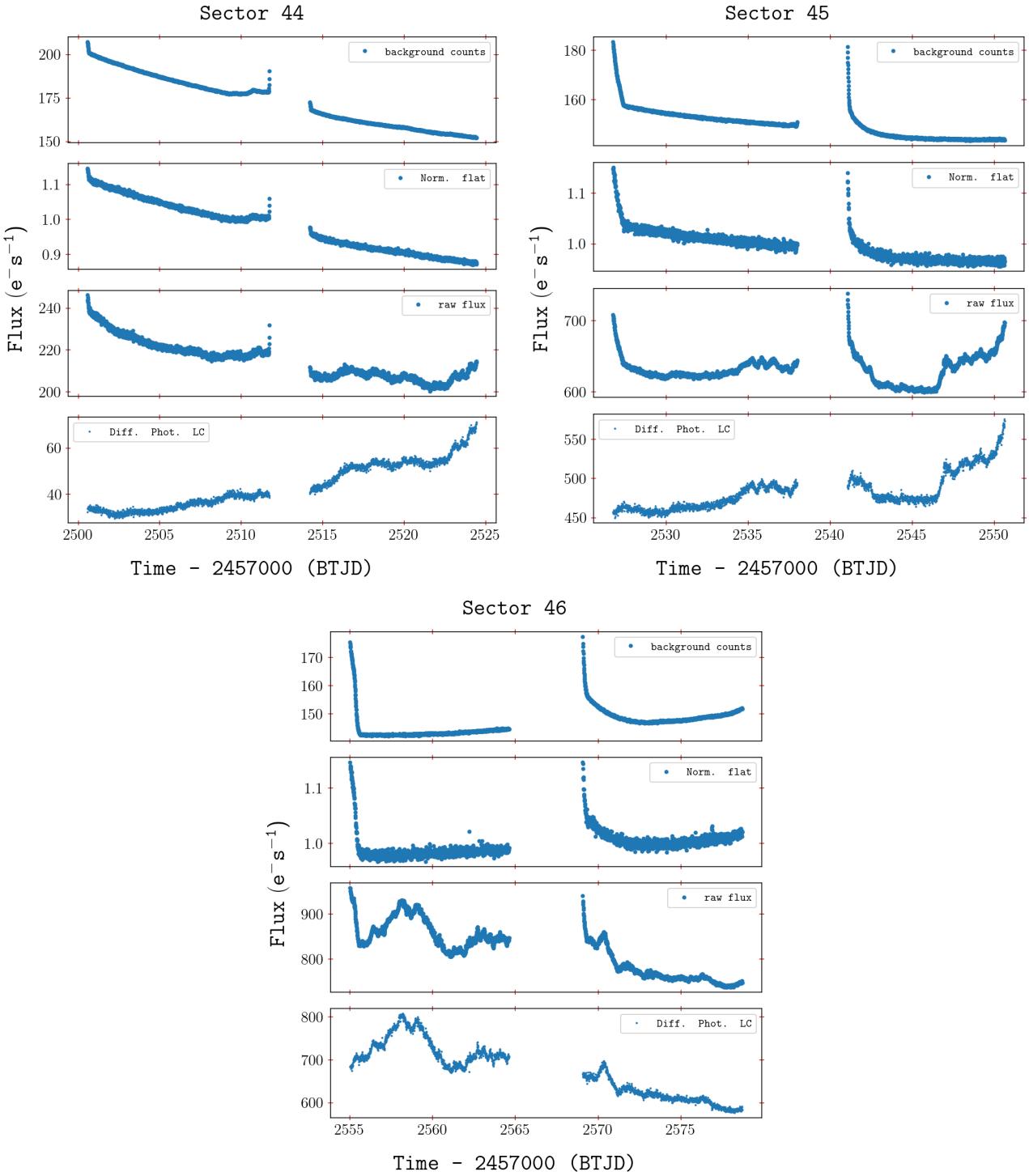


Figure A1. Each of the indicated sectors includes the flux counts obtained from the 11 × 11 full-frame image cutout. For each sector, the normalized (Norm.) flat (second panel) has been estimated using the comparison object "D" in the image cutout, where the median flux value of "D" is used for normalization. The Norm. flats under 15% only around unity have been considered for comparison of the differential LC with the LCs obtained with other methods (Figure A2). The differential photometric LC (Diff. Phot. LC, fourth panel) is then obtained by dividing the raw flux of the source by the Norm. flat.

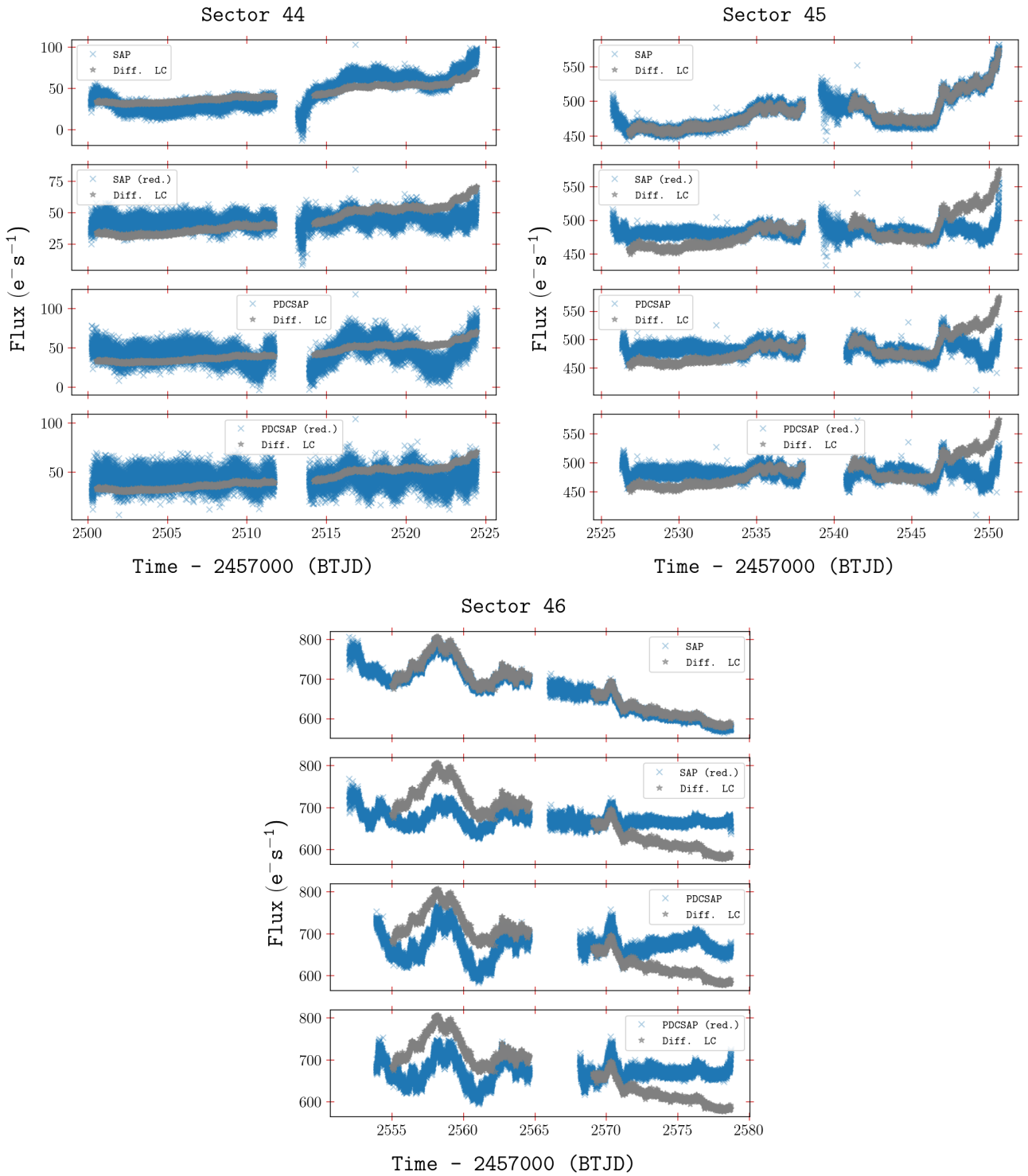


Figure A2. Comparison of the differential LC's behavior with LCs obtained with other methods. The suffix "red." denotes the corresponding flux from which long-term trending has been reduced. To visualize and compare the LC variations for each of the sectors efficiently, SAP, SAP (red.), PDCSAP, and PDCSAP (red.) LCs are shifted along the *Y*-axis so that their mean fluxes coincide with the mean of the diff. LCs.

ORCID iDs

Shubham Kishore https://orcid.org/0000-0001-8716-9412
Alok C. Gupta https://orcid.org/0000-0002-9331-4388
Debanjan Bose https://orcid.org/0000-0003-1071-5854

References

Aartsen, M. G., Ackermann, M., Adams, J., et al. 2018, AdSpR, 62, 2902
Abdo, A. A., Ackermann, M., Agudo, I., et al. 2010, ApJ, 716, 30
Acharyya, A., Adams, C. B., Archer, A., et al. 2023, ApJ, 954, 70

Aharonian, F. A. 2000, NewA, 5, 377
Ansoldi, S., Antonelli, L. A., Arcaro, C., et al. 2018, ApJL, 863, L10
Bharathan, A. M., Stalin, C. S., Sahayanathan, S., Bhattacharyya, S., & Mathew, B. 2024, MNRAS, 529, 3503
Blake, G. M. 1970, ApL, 6, 201
Britzen, S., Younsi, Z., Kun, E., et al. 2026, MNRAS, 549, stag658
Carswell, R. F., Strittmatter, P. A., Williams, R. E., Kinman, T. D., & Serkowski, K. 1974, ApJL, 190, L101
Chiaberge, M., & Ghisellini, G. 1999, MNRAS, 306, 551
Ciprini, S., Takalo, L. O., Tosti, G., et al. 2007, A&A, 467, 465
Czesla, S., Schröter, S., Schneider, C. P., et al. 2019, PyA: Python Astronomy-related Packages, Astrophysics Source Code Library, ascl:1906.010
Dawson, B. R., Fukushima, M., & Sokolsky, P. 2017, PTEP, 2017, 12A101
Dzhilkibaev, Z. A., Suvorova, O. & Baikal-GVD Collaboration 2021, ATel, 15112, 1
Emmanoulopoulos, D., McHardy, I. M., & Papadakis, I. E. 2013, MNRAS, 433, 907
Fan, J. H., Xie, G. Z., Lin, R. G., et al. 1997, A&AS, 125, 525
Fang, Y., Chen, Q., Zhang, Y., & Wu, J. 2022, ApJ, 933, 224
Filippini, F., Illuminati, G., Heijboer, A., et al. 2022, ATel, 15290, 1
Fossati, G., Maraschi, L., Celotti, A., Comastri, A., & Ghisellini, G. 1998, MNRAS, 299, 433
Garrappa, S., Buson, S., Sinapius, J., Kadler, M. & Fermi-LAT Collaboration 2021, GCN, 31194, 1
González-Martín, O., & Vaughan, S. 2012, A&A, 544, A80
Goyal, A., Gopal-Krishna, Anupama, G. C., et al. 2009, MNRAS, 399, 1622
Goyal, A., Stawarz, Ł., Ostrowski, M., et al. 2017, ApJ, 837, 127
Gupta, A. C., Banerjee, D. P. K., Ashok, N. M., & Joshi, U. C. 2004, A&A, 422, 505
Gupta, A. C., Fan, J. H., Bai, J. M., & Wagner, S. J. 2008, AJ, 135, 1384
Gupta, A. C., Gaur, H., Wiita, P. J., et al. 2019, AJ, 157, 95
IceCube Collaboration, Aartsen, M. G., Ackermann, M., et al. 2018, Sci, 361, 147
Jenkins, J. M., Twicken, J. D., McCauliff, S., et al. 2016, SPIE, 9913, 99133E
Kim, Y.-S., & Kim, J.-Y. 2025, A&A, 699, A381
Kishore, S., Gupta, A. C., & Wiita, P. J. 2023, ApJ, 943, 53
Kishore, S., Gupta, A. C., & Wiita, P. J. 2024, ApJ, 960, 11
Kishore, S., Gupta, A. C., Wiita, P. J., Mondal, S. K., & Vivek, M. 2026, MNRAS, 550, stag1284
Krishna, G., Sagar, R., & Wiita, P. J. 1995, MNRAS, 274, 701
Kouch, P. M., Lindfors, E., Hovatta, T., et al. 2026, A&A, 708, A382
Kushwaha, P., Chandra, S., Misra, R., et al. 2016, ApJL, 822, L13
Kushwaha, P., Sinha, A., Misra, R., Singh, K. P., & de Gouveia Dal Pino, E. M. 2017, ApJ, 849, 138
Kurve Collaboration, Cardoso, J. V. d. M., Hedges, C., et al. 2018, Lightkurve: Kepler and TESS Time Series Analysis in Python, Astrophysics Source Code Library, ascl:1812.013
Lister, M. L., Aller, M. F., Aller, H. D., et al. 2018, ApJS, 234, 12
Mannheim, K. 1993, A&A, 269, 67
Marshall, H. L., Liodakis, I., Marscher, A. P., et al. 2024, ApJ, 972, 74
McHardy, I. M., Koerding, E., Knigge, C., Uttley, P., & Fender, R. P. 2006, Natur, 444, 730
Mead, A. R. G., Ballard, K. R., Brand, P. W. J. L., et al. 1990, A&AS, 83, 183
Miller, H. R., Carini, M. T., & Goodrich, B. D. 1989, Natur, 337, 627
Mufakharov, T. V., Sotnikova, Y. V., Vlasyuk, V. V., et al. 2026, MNRAS, 550, stag1179
Mushotzky, R. F., Edelson, R., Baumgartner, W., & Gandhi, P. 2011, ApJL, 743, L12
Neronov, A. Y., & Semikoz, D. V. 2002, PhRvD, 66, 123003
Nilsson, K., Pursimo, T., Villforth, C., et al. 2012, A&A, 547, A1
Padovani, P., Alexander, D. M., Assef, R. J., et al. 2017, A&ARv, 25, 2
Padovani, P., Boccardi, B., Falomo, R., & Giommi, P. 2022, MNRAS, 511, 4697
Padovani, P., Oikonomou, F., Petropoulou, M., Giommi, P., & Resconi, E. 2019, MNRAS, 484, L104
Paraschos, G. F., Traianou, E., Debbrecht, L. C., Liodakis, I., & Ros, E. 2025, ApJ, 989, 208
Petkov, V. B., Novoseltsev, Y. F., Novoseltseva, R. V. & Baksan Underground Scintillation Telescope Group 2021, ATel, 15143, 1
Pierre Auger Collaboration, Aab, A., Abreu, P., et al. 2017, Sci, 357, 1266
Plavin, A. V., Kovalev, Y. Y., Kovalev, Y. A., & Troitsky, S. V. 2021, ApJ, 908, 157
Prince, R., Das, S., Gupta, N., Majumdar, P., & Czerny, B. 2024, MNRAS, 527, 8746
Qian, B., & Tao, J. 2004, PASP, 116, 161
Raiteri, C. M., Villata, M., Carosati, D., et al. 2021, MNRAS, 501, 1100
Revalski, M., Nowak, D., Wiita, P. J., Wehrle, A. E., & Unwin, S. C. 2014, ApJ, 785, 60
Ricker, G. R., Winn, J. N., Vanderspek, R., et al. 2014, SPIE, 9143, 914320
Sahakyan, N., Giommi, P., Padovani, P., et al. 2023, MNRAS, 519, 1396
Shah, Z., Jithesh, V., Sahayanathan, S., & Iqbal, N. 2021, MNRAS, 504, 416
Shimizu, T. T., & Mushotzky, R. F. 2013, ApJ, 770, 60
Smith, K. L., Mushotzky, R. F., Boyd, P. T., et al. 2018, ApJ, 857, 141
Smith, P. S., Balonek, T. J., Heckert, P. A., Elston, R., & Schmidt, G. D. 1985, AJ, 90, 1184
Takalo, L. O. 1991, A&AS, 90, 161
Takalo, L. O., Sillanpaa, A., Nilsson, K., et al. 1992, A&AS, 94, 37
Tommasi, L., Palazzi, E., Pian, E., et al. 2001, A&A, 376, 51
Twicken, J. D., Caldwell, D. A., Jenkins, J. M., et al. 2020, TESS Science Data Products Description Document EXP-TESS-ARC-ICD-0014 Rev F, NASA/TM—20205008729, https://archive.stsci.edu/files/live/sites/mast/files/home/missions-and-data/active-missions/tess/_documents/EXP-TESS-ARC-ICD-TM-0014-Rev-F.pdf
Urry, C. M., & Padovani, P. 1995, PASP, 107, 803
Uttley, P., McHardy, I. M., & Papadakis, I. E. 2002, MNRAS, 332, 231
Uttley, P., McHardy, I. M., & Vaughan, S. 2005, MNRAS, 359, 345
Valtaoja, L., Karttunen, H., Efimov, Y., & Shakhovskoy, N. M. 1993, A&A, 278, 371
Valtaoja, L., Sillanpaa, A., Valtaoja, E., Shakhovskoi, N. M., & Efimov, I. S. 1991, AJ, 101, 78
Vaughan, S. 2005, A&A, 431, 391
Vaughan, S. 2010, MNRAS, 402, 307
Vaughan, S., Edelson, R., Warwick, R. S., & Uttley, P. 2003, MNRAS, 345, 1271
Virtanen, P., Gommers, R., Oliphant, T. E., et al. 2020, NaMet, 17, 261
Wagner, S. J., & Witzel, A. 1995, ARA&A, 33, 163
Wills, B. J., Wills, D., & Breger, M. 2011, ApJS, 194, 19
Zechmeister, M., & Kürster, M. 2009, A&A, 496, 577